AIAA JOURNAL
Vol. 46, No. 7, July 2008

Numerical Study on the Unsteady-Force-Generation Mechanism of Insect Flapping Motion

Jung-Sang Lee,* Jin-Ho Kim,† and Chongam Kim‡
Seoul National University, Seoul 151-742, Republic of Korea

DOI: 10.2514/1.35646

Detailed numerical simulations are conducted to investigate aerodynamic characteristics of unsteady-force generation by a two-dimensional flapping motion under a forward-flight condition. A realistic wing trajectory called the figure-eight motion is extracted from a blowfly's tethered flight under freestream. Computed results show complex vortical flowfields that exhibit very interesting and distinctive unsteady characteristics. Lift is mainly generated during downstroke motion by a high effective angle of attack due to translational and lagging motion. On the other hand, a large amount of thrust is abruptly generated at the end of upstroke motion. Vortical structure in the wake and the pressure field shows that vortex-pairing and vortex-staying mechanisms can be presented as strong evidence for the abrupt large thrust generation, which is fundamentally different from the inverse Kármán vortex that is used to explain thrust generation by sinusoidal oscillating airfoil. Additional numerical simulations are conducted to examine the effects of motion components of figure-eight motion. From numerical results and comparisons, it is observed that wing rotational motion at the end of upstroke is crucial in generating the pairing and staying of vortices, which eventually leads to the abrupt thrust generation.

Nomenclature

C_d	=	drag coefficient
C_l	=	lift coefficient
C_t	=	thrust coefficient ($-C_d$)
c	=	chord length
f	=	frequency in hertz
k	=	reduced frequency in terms of c ($fc/U_{\max}$)
Re	=	Reynolds number ($U_{\max}c/\nu$)
U_∞	=	freestream velocity
$U_{\max}$	=	maximum relative velocity
$x(t)$	=	lagging motion (horizontal direction motion)
$y(t)$	=	translational motion (vertical direction motion)
t	=	nondimensional time
$\alpha(t)$	=	rotational motion
ν	=	freestream kinematic viscosity
τ	=	pseudotime

Introduction

FLAPPING motion has been considered as a fascinating aerodynamic subject to many scientists and engineers because of its potential applicability to various propulsive devices or next-generation micro aerial vehicles. To uncover its curious unsteady behavior, many researchers have conducted experimental or computational studies on the unsteady aerodynamics of various flapping motions such as periodic oscillating airfoils, an insect's and/or a bird's wing motions, and so on.

Koochesfahani [1] showed various vortical flow patterns of the inverse Kármán vortex behind a periodic pitching airfoil and measured thrust using a time-averaged velocity profile in the wake. Anderson et al. [2] also visualized the flowfield around an oscillating (combined pitching and heaving motion) airfoil and measured the performance index, such as thrust generation or propulsive efficiency. They investigated effects of flow pattern on flapping performance and classified principal flow characteristics. Aside from experimental studies, numerical simulations also contributed to finding the role of vortices in flapping airfoil. Isogai et al. [3] conducted numerical simulation using a compressible Navier–Stokes code, and they observed that large-scale vortices around the upper airfoil surface could make a lift enhancement, but could deteriorate propulsive efficiency. Tuncer and Platzer [4] made numerical flow visualization using a particle-tracing technique and studied the effects of unsteady vortices on a flapping airfoil. In addition, Mustafa and Tuncer [5] investigated an optimal path of a flapping airfoil to improve the maximum thrust and propulsive efficiency. Based on the physical interpretation of various vortical structures, Lee et al. [6] designed an optimal flapping airfoil sustaining a high propulsive efficiency and a high thrust coefficient. Platzer and Jones [7] gave a valuable review on recent developments in the understanding and prediction of flapping-wing aerodynamics. The recent mathematical and physical modeling of the flows around flapping wings can also be found in a comprehensive review by Rozhdestvensky and Ryzhov [8].

As already mentioned, it is the pattern of vortical flows that plays an important role in generating unsteady aerodynamic forces and determining the efficiency of flapping motion. Thus, detailed analysis of vortical structure should be carried out to physically understand unsteady flapping aerodynamics. Moreover, it has been reported that conventional aerodynamics based on quasi-steady assumption could not be applied to an insect's flapping motion [9].

The vortex in an insect's flapping motion (or the figure-eight motion) yields favorable aerodynamic consequences. It can produce a sufficiently large amount of lift using the dynamic stall phenomenon. Ellington et al. [10] observed the leading-edge vortex (LEV) using smoke visualization around both a real moth and a three-dimensional (3-D) model called *flapper* at a Reynolds number $\mathcal{O}(10^3)$. They observed a strong vortex attached at the leading edge of a wing in downstroke motion. As another unsteady-lift-enhancement mechanism, a vortical pattern produced by the clap-fling motion [11] was observed. Recently, Sun and Yu [12] numerically simulated a two-dimensional (2-D) clap-fling motion of a tiny insect using a Navier–Stokes solver, and they showed that a sufficiently large amount of lift could be generated.

Presented as Paper 3210 at the 36th Fluid Dynamics Conference and Exhibit, San Francisco, California, 5–8 June 2006; received 13 November 2007; revision received 27 February 2008; accepted for publication 5 March 2008.

*Ph.D., School of Mechanical and Aerospace Engineering, Department of Aerospace Engineering.

†Graduate Student, Ph.D. Candidate, School of Mechanical and Aerospace Engineering, Department of Aerospace Engineering.

‡Associate Professor, School of Mechanical and Aerospace Engineering, Institute of Advanced Aerospace Technology; chongam@snu.ac.kr. Senior Member AIAA.

In addition to those vortical effects, there are other unsteady effects closely related to an insect's hovering. Dickinson et al. [13] observed two important lift-enhancement mechanisms using a mechanical model of an insect's hovering called *robofly*. The first mechanism, called *rotational circulation*, is analogous to the Magnus effect observed in a rotating circular cylinder. The second mechanism, called *wake capture*, results from the interaction between the wing and the vortex shed by the wing rotation. Other interesting aspects of an insect's hovering motion can be found in the review papers [14,15].

Although previous works could explain many interesting aspects of flapping motions, further study is necessary to understand unsteady flowfields of flapping motion under the forward-flight condition. An airfoil under sinusoidal flapping (or combined pitching and heaving) motion [1–6] cannot produce a net lift for hovering. On the other hand, unsteady mechanisms in an insect's hovering need to be verified for more general flight conditions such as forward flight and rapid maneuvering. Rapid maneuvering, which is one of the most vivid characteristics in insect flight, has to be carefully examined to design highly maneuverable flapping micro aerial vehicles.

The flapping model is chosen as a 2-D blowfly's wing motion, called the *figure-eight motion*, under forward-flight conditions. It is extracted from the results of Nachtigall's [16] tethered-flight experiment. Although the present computation is limited to the 2-D analysis of the tethered-flight wing motion, the results show very interesting and distinctive unsteady aerodynamic characteristics, which would be valuable information to understand its 3-D counterpart. Moreover, it was reported in hovering flight that 2-D characteristics were not too much different from the 3-D case [17,18]. Numerical results show that positive lift is mostly generated during downstroke, but thrust is produced abruptly when insect wings rotate at the end of upstroke. By examining the unsteady-flow feature and computed aerodynamic force, it is observed that the large amount of lift is produced by a high effective angle of attack due to translational/lagging motion. Moreover, it is found that the abrupt thrust generation is closely related to a vortex pairing in the velocity field and a vortex staying in the pressure field, which is caused by the rotational component of figure-eight motion.

The present paper is organized as follows. First, numerical methods and modeling of flapping motion are introduced. Then detailed numerical investigations of figure-eight motion are carried out in terms of the stroke and motion component. Finally, the role of vortex interaction in unsteady-aerodynamic-force generation is examined and its relationship with rotational circulation is clarified.

Numerical Methods

Governing Equations

Because of low Reynolds number flow characteristics, the 2-D unsteady incompressible Navier-Stokes equations are employed as the governing equations.

$$\frac{\partial \mathbf{v}}{\partial t} + \mathbf{v} \cdot \nabla \mathbf{v} + \nabla p = \nabla \cdot \sigma \tag{1}$$

$$\nabla \cdot \mathbf{v} = 0 \tag{2}$$

where p denotes the pressure, and $\mathbf{v} = \mathbf{v}_a + \mathbf{w}$ is the flow velocity, where $\mathbf{v}_a$ is the convection velocity, $\mathbf{w}$ is the mesh velocity to present figure-eight motion, and σ is the stress tensor. Both pressure and stress tensors are normalized by density.

The artificial-compressibility method is employed to iteratively update velocity and pressure fields by satisfying the momentum equation (1).

$$\frac{\partial p}{\partial \tau} = -\beta \nabla \cdot \mathbf{v} \tag{3}$$

Upwind-biased Osher's flux-difference splitting is used for spatial discretization [19]. A third-order linear variable reconstruction is employed to attain a higher-order spatial accuracy. For time integration, the lower–upper symmetric Gauss–Seidel scheme is used with the dual-time-stepping method. The final discretized form of the governing equations can be shown as

$$\left[\frac{I}{J\Delta\tau} + \left(\frac{\partial \hat{R}}{\partial Q} + \frac{\partial \hat{S}}{\partial Q}\right)^{n+1,m}\right] \Delta Q^{n+1,m} = -(\hat{R}^{n+1,m} + \hat{S}^{n+1,m}) \tag{4}$$

where superscript n indicates the physical time level, m denotes the pseudotime iteration, R is the residual vector including inviscid and viscous fluxes, $\hat{S}$ is an unsteady-source-like term, Q is the flow variable vector, and J is the Jacobian. Detailed numerical implementation including spatial discretization and time integration can be found in [19,20].

Boundary conditions for the inflow and outflow regions are based on the method of characteristics. At inflow, the velocity component is specified from the freestream condition and pressure is extrapolated from interior grid points. At outflow, pressure is specified and the velocity component is determined by extrapolation. The velocity component is an approximate Riemann invariant corresponding to the characteristic wave. On the solid wall, velocity is the same as airfoil velocity, to simulate time-dependent motion. Because the Reynolds number in this work is relatively low [$Re = \mathcal{O}(10^3)$], all computations are conducted under the fully laminar flow assumption. To relieve computing load in unsteady viscous flow calculation, standard parallel computing technique by message-passing-interface programming has been implemented. The present numerical methods and code have been extensively validated in various steady and unsteady flows by Kim et al. [20] and compared with the experiment [1,2] of sinusoidal flapping airfoils by Lee et al. [6]

Numerical Modeling of a 2-D Insect Flapping Motion

It is difficult to precisely measure wing motion under free-flight conditions [15]. Thus, a tethered-flight experiment is usually conducted as an alternative to track wing trajectory, and it may properly mimic forward-flight conditions by superposing freestream velocity.

Several researchers have measured wing trajectories by using a wind tunnel and a high-speed-camera system [15–17]. Nachtigall [16] suspended a blowfly in front of an open wind tunnel and adjusted wind speed until the net horizontal force acting on the blowfly is zero to realize the forward-flight condition. In 2-D side view, the wing-tip trajectory of many insects looks like the figure eight (thus, the so-called figure-eight motion) [15,21]. Nachtigall's [16] experiment also exhibited the figure-eight motion of the blowfly wing, for which the trajectory can be expressed in terms of the Fourier series.

$$F(t) = a_0 + \sum_{n=1}^{m} a_n \cos(2n\pi kt) + b_n \sin(2n\pi kt) \tag{5}$$

$$F(t) = [x(t), y(t), \alpha(t)]^T \tag{6}$$

where a_0, a_n, and b_n are Fourier coefficients. Detailed coefficients can be found in [22]. Figure 1 shows that the wing-tip trajectory consists of three components: translation [$y(t)$, vertical motion], lagging [$x(t)$, horizontal motion], and rotation [$\alpha(t)$]. From the airfoil trajectory measured at equal time intervals, the overall characteristics of the figure-eight motion can be easily observed. The wing translates relatively slowly during downstroke and its posture is approximately horizontal; thus, rotation is not severe. On the other hand, upstroke motion is fast and the leading edge is sharply pitched up. Rapid wing rotation is mainly concentrated near the end of upstroke. As shown in Fig. 1, the directions of lift and thrust are the same as those of Nachtigall's [16] experiment.

Numerical Results

There are several ways to define the Reynolds number of an insect's flapping motion [21]. Sometimes, the conventional way of

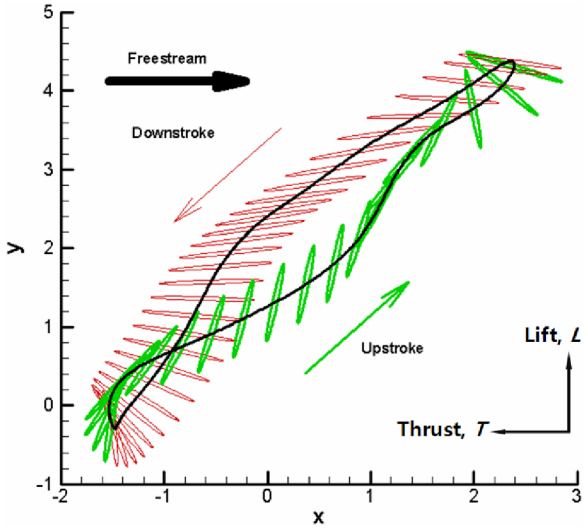

Fig. 1 Nondimensional position of a blowfly's wing element during tethered flight: downstroke phase and upstroke phases.

defining the Reynolds number for fixed-wing aircraft may not be appropriate. For example, the Reynolds number based on freestream velocity cannot be defined in the case of insect hovering. To avoid any confusion, the Reynolds number in the present work is defined by using the maximum relative velocity of wing motion instead of freestream velocity.

$$Re = \frac{U_{\max} c}{\upsilon} \tag{7}$$

All of the computed aerodynamic coefficients are normalized by the maximum relative speed, as in Eq. (8).

Table 1 Simulation data from Nachtigall [16]

Airspeed U_∞	2.7 m/s
Maximum relative speed $U_{\max}$	9.963 m/s
Chord length c	3.8 mm
Reynolds number Re_c	2523.92
Rotation center	10% of chord
Flapping frequency f	130.6 Hz
Reduced frequency k	0.049813

$$c_i = \frac{F_i}{\frac{1}{2} c \rho U_{\max}^2} \tag{8}$$

where F_i is lift or thrust force, and c and ρ are the chord length and density, respectively. As shown in Table 1, flow conditions (including nondimensional numbers necessary for numerical computation) can be obtained from Nachtigall's [16] experimental data.

For the sake of simplicity, the wing sectional shape is assumed to be a very thin elliptical airfoil for which the maximum thickness is 5% of the chord length. A 221×97 size O-grid with the wall spacing of 4×10^{-4} chord is used, and the outer boundary of the computational domain extends to 25 chords. As can be seen in Figs. 2–4 (rotational motion will be described with the motion-component effect), the fundamental unsteady aerodynamic characteristics do not change in computations using a fine grid (385×161, about three times denser than the baseline grid). All computations were carried out for 10 cycles to obtain sufficient periodic behavior of aerodynamic coefficients. The physical time step is obtained by dividing one cycle into 1000 subintervals. At each physical time step, pseudoiterations are carried out until both the maximum divergence of velocity and the maximum residual are less than 5×10^{-6}.

Figures 2 and 3 show histories of instantaneous lift and thrust coefficients. Downstroke and upstroke is indicated by the white and gray regions, respectively. Aerodynamic coefficients highly

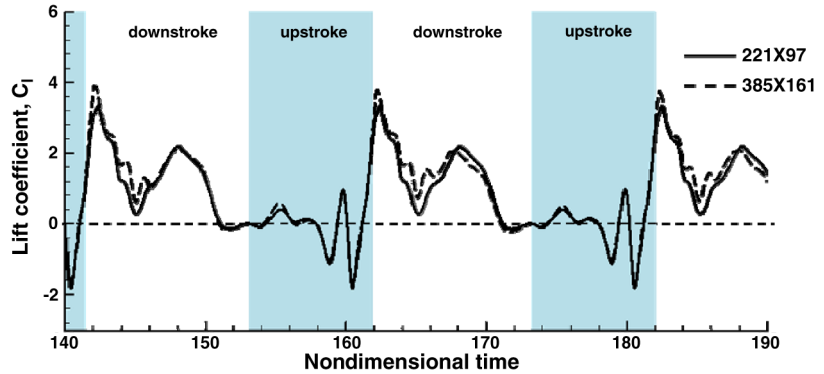

Fig. 2 History of the instantaneous lift coefficient of figure-eight motion.

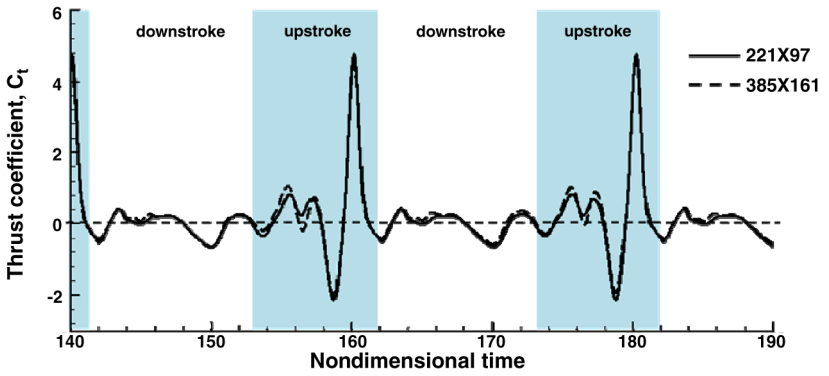

Fig. 3 History of the instantaneous thrust coefficient of figure-eight motion.

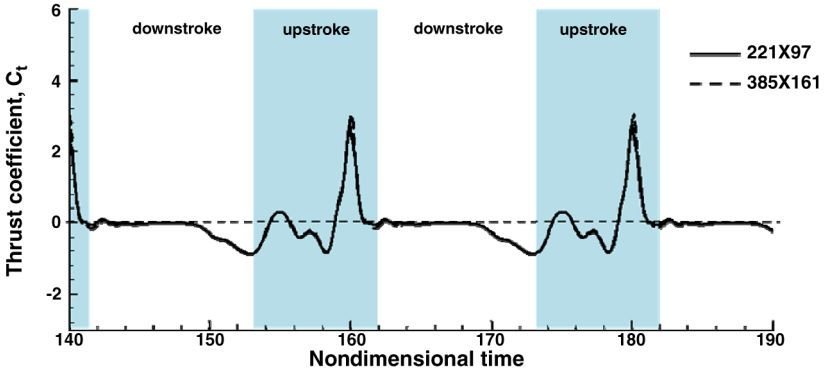

Fig. 4 History of the instantaneous thrust coefficient of rotational motion only.

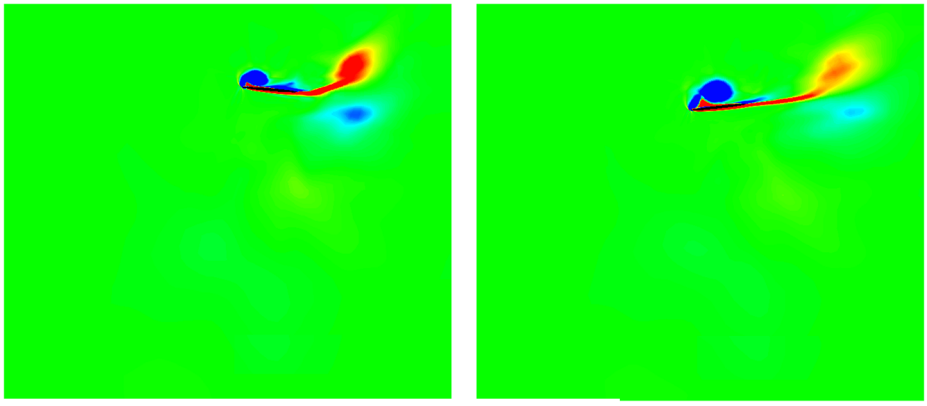

a) t=162.608 b) t=163.210

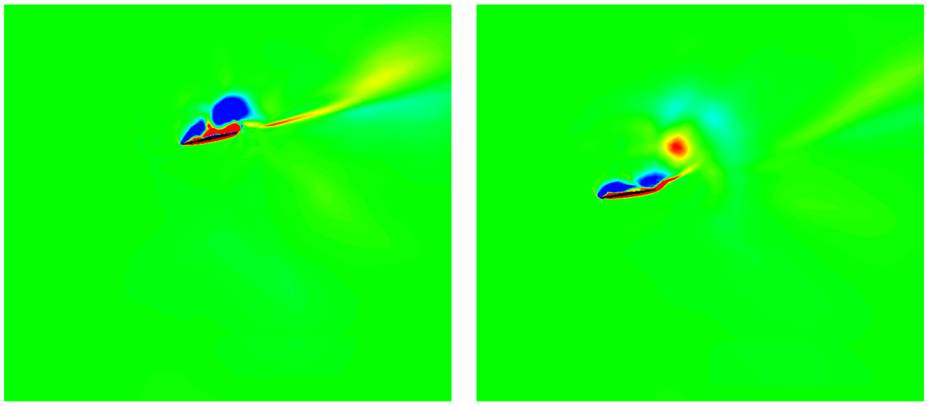

c) t=164.214 d) t=166.824

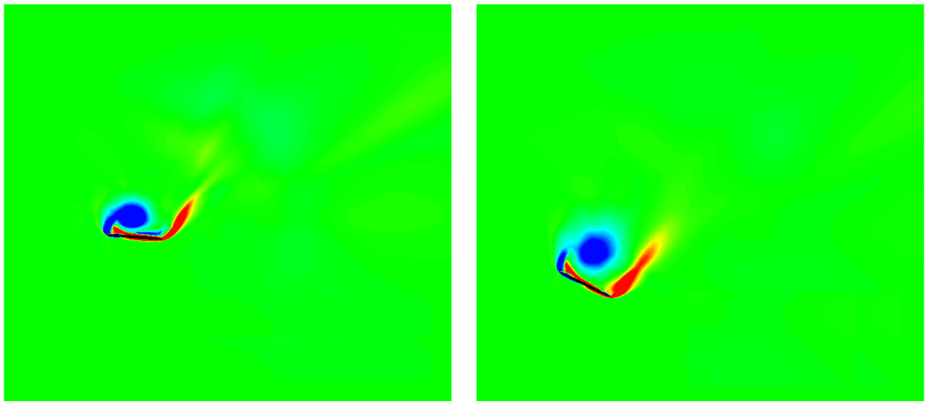

e) t=168.430 f) t=170.036

Fig. 5 Vorticity contours during downstroke.

fluctuate and high peak values are obtained (the instantaneous maximum lift coefficient is 3.355, the instantaneous maximum thrust coefficient is 4.79). The mean lift and thrust coefficients, which could be evaluated by Eq. (9), are 0.689 and 0.146, respectively.

$$\bar{c}_i = \frac{1}{T}\int_0^T c_i \, dt \tag{9}$$

where c_i is instantaneous aerodynamic coefficient, T is the time of one period, and the overbar denotes the mean value. Because experimental data of the present figure-eight motion were measured when the net average horizontal force was zero, the time-averaged thrust can be regarded as the time-averaged drag. With this condition, the lift-to-drag (or the absolute value of thrust) ratio L/D is obtained as 4.719.

From Figs. 2 and 3, it is clear that lift is mainly generated during downstroke motion, whereas thrust is produced abruptly at the end of upstroke. Thus, the physical relationship between flow feature and

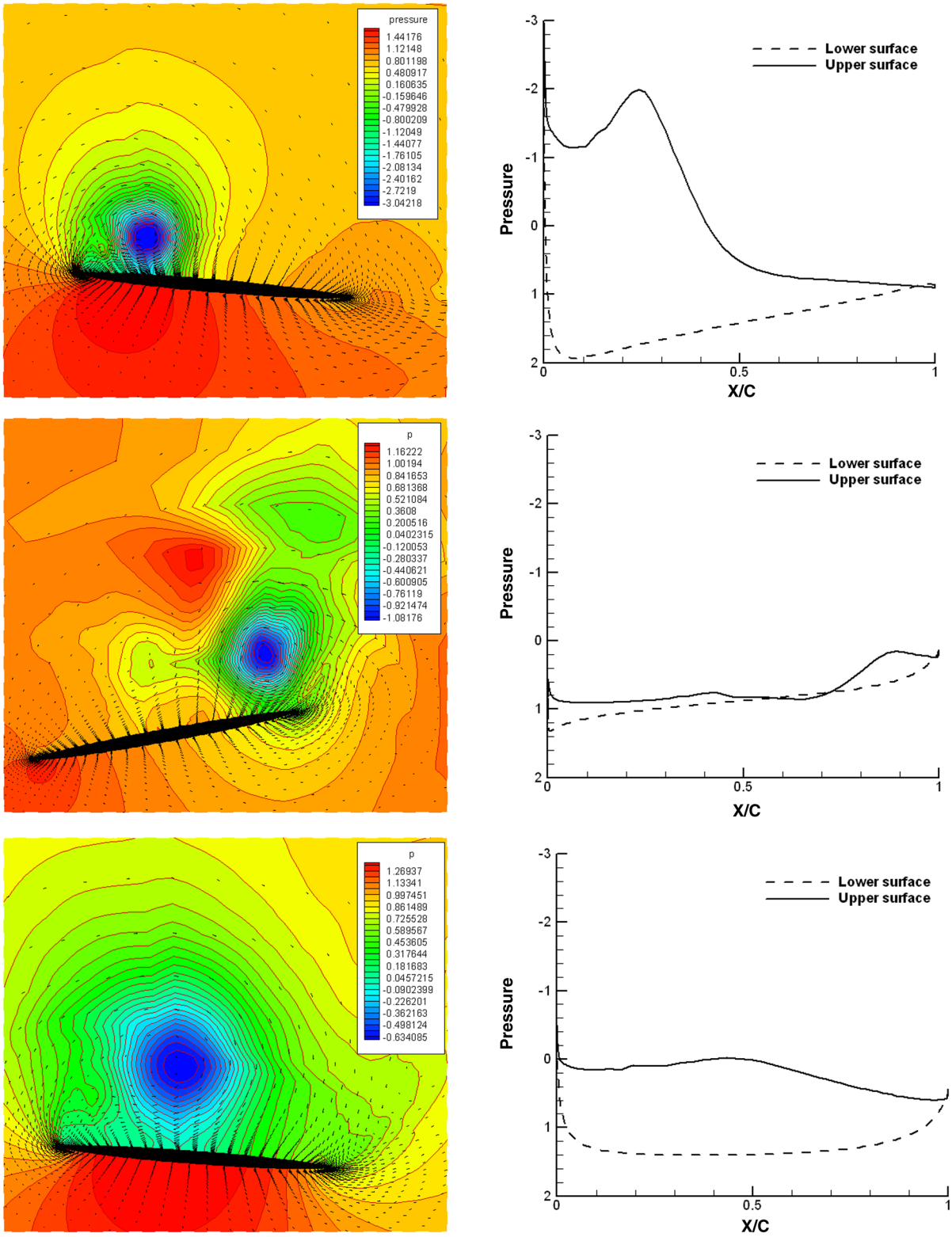

Fig. 6 Leading-edge vortex at $t = 162.608$ (top), 165.017 (middle), and 168.430 (bottom) for the pressure and velocity vector fields (left) and pressure distribution on the wall (right).

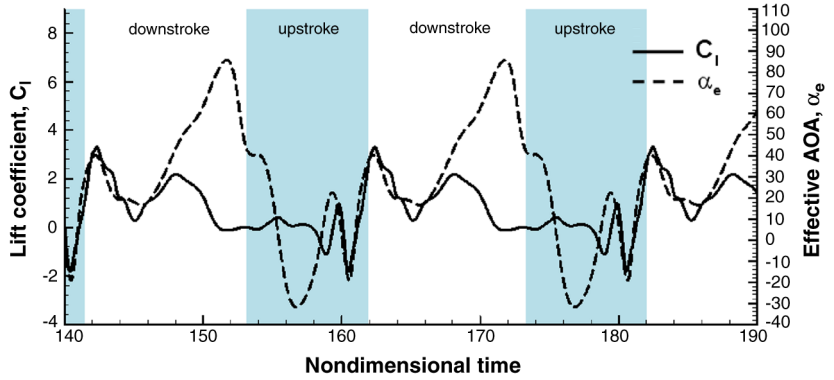

Fig. 7 Effective angle of attack versus lift coefficient.

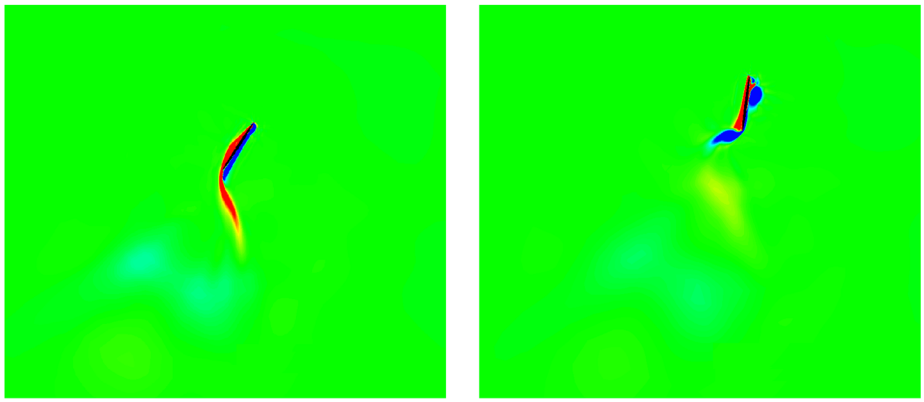

a) t=179.036 **b) t=180.073**

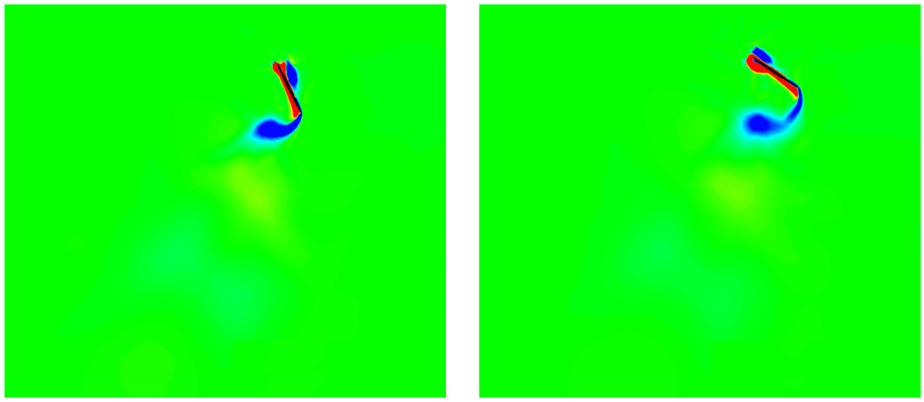

c) t=180.479 **d) t=180.876**

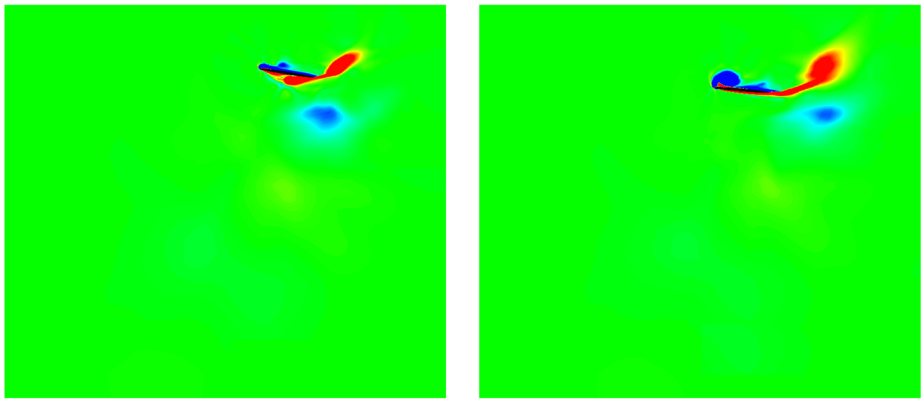

e) t=182.081 **f) t=182.683**

Fig. 8 Vorticity contours during upstroke.

aerodynamic-force generation is investigated by splitting the down- and upstroke motions.

Downstroke

It is well known that the vortical flow over the airfoil is responsible for a large lift generation [10,13]. In Fig. 2, there are two peaks of lift coefficient at around $t = 163$ and 168. To see the role of the LEV in lift enhancement, vorticity and pressure fields are examined. Figure 5 shows snapshots of the vorticity field, illustrating the formation and shedding of vortices at the leading and trailing edges. At the early downstroke, a vortex develops at the leading edge (Figs. 5a and 5b) and the first peak of lift coefficient appears (Fig. 2). The LEV sheds into the wake (Fig. 5c). A new vortex is then developed at the leading edge (Figs. 5d and 5e) and the second peak of lift coefficient appears (Fig. 2). Finally, the new vortex also sheds from the leading edge (Fig. 5f). At this moment, lift coefficient is being decreased.

Figure 6 shows the pressure and velocity fields around an airfoil at $t = 162.608$ (the first peak), 165.017, and 168.430 (the second peak) when the instantaneous lift coefficient reaches local maximum values. It is clearly seen that the location of the LEV center in the left figure and that of pressure suction peak in the right figure are identical. Thus, the instantaneous lift-enhancement results from the lower pressure distribution due to the LEV.

As shown in Fig. 2, the fluctuation of lift coefficient comes from the development and shedding of the LEV. According to several studies on normal hovering, vortex shedding at the leading and trailing edges is known as a specific phenomenon in 2-D analysis [15,17]. In 3-D analysis, however, the leading-edge vortex is stably attached, and thus lift coefficient does not fluctuate as in the 2-D case [14,15,23]. Recently, Wilkins and Knowles [23] numerically studied the stability of the LEV for various Reynolds numbers. They observed that the LEV was detached in all 2-D computations except for those with very low Reynolds number. However, it has been reported that the average lift coefficient in the 3-D case was only about 20% less than with the 2-D case [17]. It implies that computed aerodynamic forces for 2-D and 3-D flapping motions did not show remarkable differences, despite a substantial difference in the LEV structure. From this point of view, the present 2-D computation is valuable in itself in examining aerodynamic differences between 2-D and 3-D forward-flight motions.

Another important feature observed in the present work is that, unlike the normal hovering flight, the figure-eight motion of the present forward flight can generate a large amount of lift without producing drag.

The stroke path of the insect wing in normal hovering is almost horizontal, but it maintains a high geometric angle of attack to produce a large-scale LEV [13,23]. In the case of the present forward flight, as shown in Figs. 5 and 6, the LEV development and the lift enhancement appear at low (or even negative) geometric angles of attack. The LEV is formed by the effective angle of attack, not by the geometric angle of attack [3]. The effective angle of attack is defined by

$$\alpha_e = \alpha + \tan^{-1}\frac{-v'}{U_\infty - u'} \tag{10}$$

From Eq. (10), even at a low geometric angle of attack, a high effective angle of attack may be induced by lagging (negative u') or translational (negative v') velocity. Figure-eight motion in a forward flight exploits an effective angle of attack, instead of a geometric angle of attack, to produce the LEV. As shown in Fig. 7, the effective angle of attack around the two peaks of lift coefficient is high, confirming that most lift generation during downstroke is due to vortex generation by a high effective angle of attack. This is consistent with the previous observation that the effective angle of attack plays an important role in generating the leading-edge vortex [3,4]. After the second peak, however, there is substantial deviation. The reason is that the wing is rapidly changing its direction and then it is almost perpendicular to the freestream direction. Thus, it cannot generate lift. Conclusively, high lift implies a high effective angle of attack, but a high effective angle of attack does not always imply high lift in figure-eight motion. Aerodynamically, using the effective angle of attack for the forward flight is particularly efficient because a substantial amount of drag would be created by the LEV if the wing maintains a high geometric angle of attack, which would make the forward flight almost impossible. This result can be beneficially applied in the wing design of flapping micro aerial vehicles.

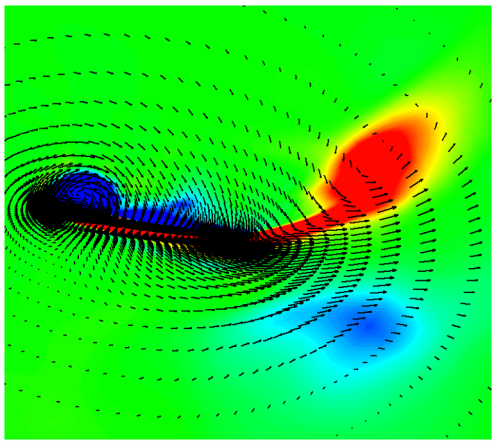

Fig. 9 Vortex pairing and a jet flow in the wake.

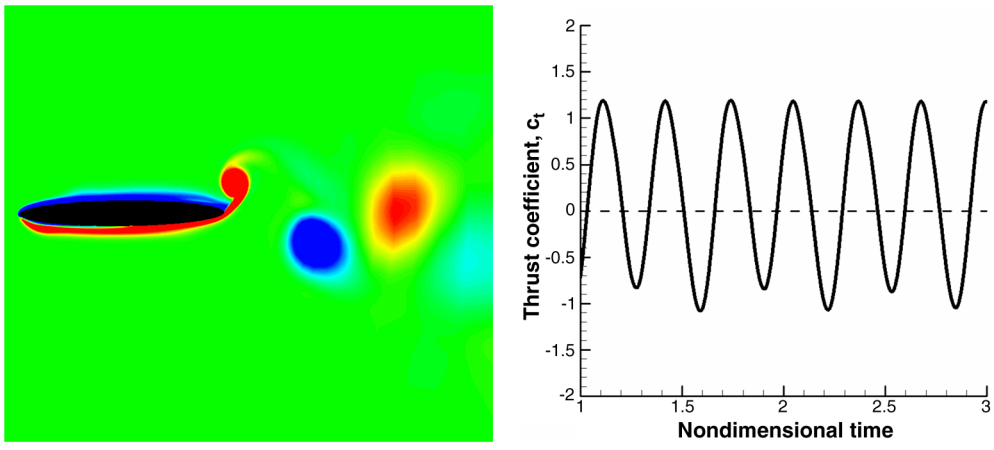

a) **b)**

Fig. 10 Pitching airfoil: a) inverse Kármán vortex street and b) history of the thrust coefficient ($Re = 12,000$, pitching amplitude is 10 deg, $k = 10$, maximum thickness is 12% of the chord length).

Upstroke

To understand the aerodynamic mechanism of the abrupt thrust generation in Fig. 3, vorticity fields are examined at the end of upstroke. Figure 8 shows sequential vorticity contours at the end of upstroke (from $t = 179.069$ to 182.683). The airfoil starts to rotate counterclockwise (Fig. 8a), and the clockwise-rotating vortex is shedding from the shear layer at the trailing edge (Fig. 8b). The vortex completely sheds from the airfoil (Fig. 8c) and then it stays for a while at the same position (Fig. 8d). At the end of rotation, a new counterclockwise rotating vortex develops again from the shear layer at the trailing edge (Fig. 8e). Finally, the two vortices form a pairing and move into the downstream (Fig. 8f). As a close-up view of Fig. 8f, Fig. 9 describes velocity and vorticity fields in the wake region. It clearly shows that the two vortices vertically align and a

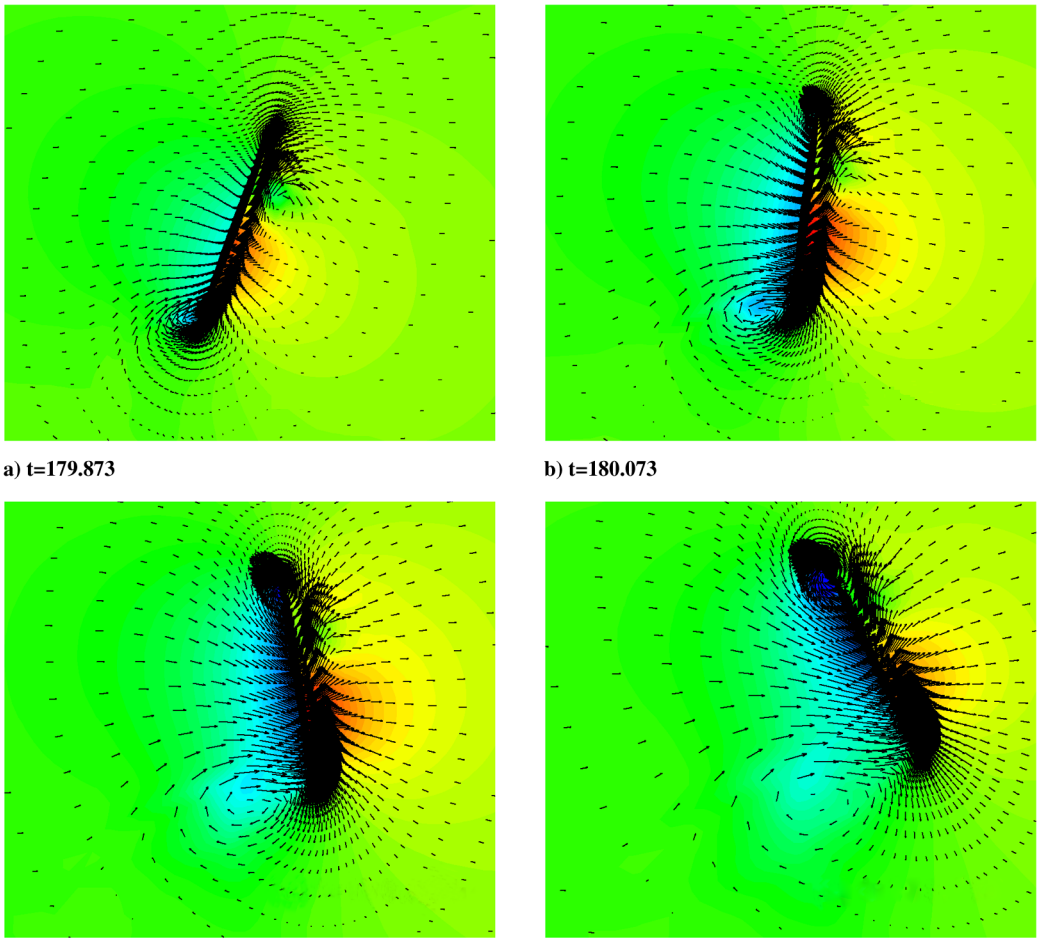

a) t=179.873 **b) t=180.073**

c) t=180.274 **d) t=180.479**

Fig. 11 Pressure and velocity vector field near the maximum thrust coefficient.

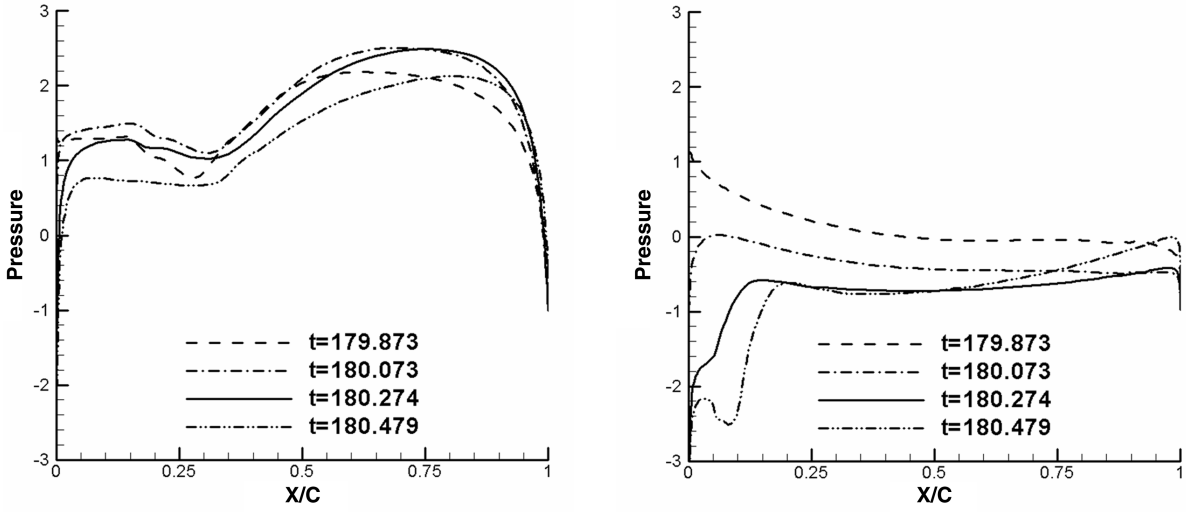

a) **b)**

Fig. 12 Surface pressure distribution: a) upper surface (rear side) and b) lower surface (front side).

strong jet is induced between the two vortices. Transverse momentum induced by the jet contributes to the abrupt thrust generation. The vortex pairing and formation of the jet flow could also be explained by the vortex system. When pairing vortices form a vortex system such as that shown in Fig. 9, the net velocity field near two vortices can be obtained as a superposition of each velocity field [24]. Because the lower vortex rotates clockwise and the upper vortex rotates counterclockwise, the resultant velocity field is a strong transverse jet flow.

In summary, the strong transverse jet that induces the abrupt thrust generation comes from the interaction of two opposite rotating vortices, and this vortex-pairing mechanism is abruptly developed at the end of upstroke.

Although a similar thrust generation can be seen in sinusoidal flapping motion, the strong transverse jet due to the vertical vortex pairing cannot be observed. In sinusoidal flapping motion, thrust force is generated by a periodic vortex shedding called an inverse Kármán vortex street [1,4]. Figure 10 shows an inverse Kármán vortex street and thrust-generation pattern by a pitching airfoil. Unlike in Fig. 9, shedding vortices are not aligned vertically, and thus an instantaneous strong jet in the transverse direction is not produced. It appears that the vortex pairing and formation of a transverse jet is a phenomenon that is particularly observed in the figure-eight motion for the abrupt thrust generation. Extension of the present thrust-generation mechanism to 3-D figure-eight motion, however, requires detailed computational or experimental validation.

Figure 11 shows the pressure and velocity distribution over an airfoil at around $t = 180.254$, when thrust becomes maximal. A clockwise vortex develops from the upper shear layer of the trailing edge (Fig. 11a). At the same time, a small vortex is created at the upper leading edge. The trailing-edge vortex takes part in the vortex-pairing phenomenon. As the airfoil rotates, velocity vectors increasing in magnitude indicate rapid flow acceleration at the lower surface of the airfoil (Figs. 11c and 11d). Flow around the leading and trailing edges is being sucked into the airfoil. A wide region of low pressure is then developed, whereas pressure at the upper surface of the airfoil is relatively high: as a result, thrust is created. Again, the airfoil rotation plays a critical role in inducing the large pressure difference.

The temporal evolution of pressure distribution at the upper and lower surfaces of the airfoil is shown in Fig. 12. At the upper surface, pressure is increasing from $t = 179.873$ to 180.479. From $t = 180.073$ to 180.274, thrust becomes maximal, and pressure distribution does not change much. At $t = 180.479$, pressure starts to decrease. On the other hand, pressure at the lower surface continuously decreases. Even at $t = 180.479$, when pressure at the

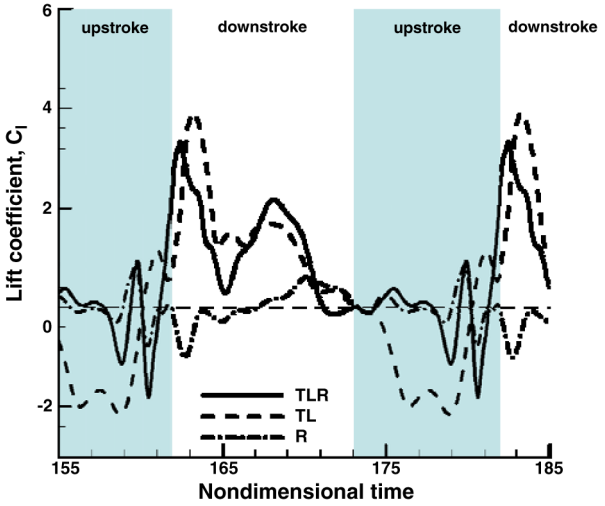

Fig. 13 Lift generation according to the motion component (TLR denotes translation, lagging, and rotation of figure-eight motion; TL denotes translation/lagging motion; and R indicates rotation-only motion).

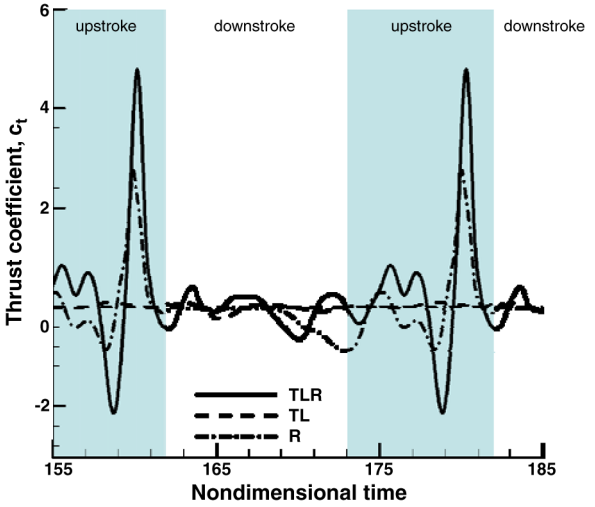

Fig. 14 Thrust generation according to the motion component (TLR denotes translation, lagging, and rotation of figure-eight motion; TL denotes translation/lagging motion; and R indicates rotation-only motion).

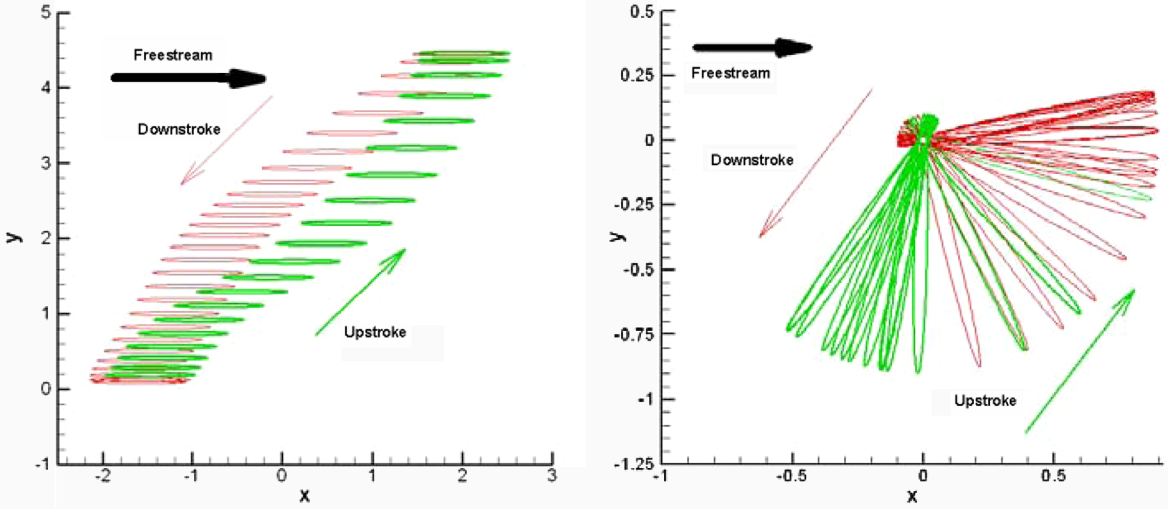

Fig. 15 Translational and lagging motion (left) and rotation only (right).

upper surface starts to decrease, pressure at the lower surface remains lower. This is definitely due to the vortex staying at the lower surface of the airfoil. The vortex at the lower surface does not immediately move to the downstream side, but stays for a while at the same position, creating a lower-pressure zone. As a result, substantial a pressure difference across the airfoil surface is maintained.

The vortex-staying phenomenon seems to be somewhat different from the wake capturing observed by Dickinson et al. [13] Although the wake capturing mainly changes flow direction to produce additional lift, the vortex staying maintains a lower-pressure zone for a relatively long time, to produce thrust.

Together with hovering, rapid maneuvering is one of the most vivid aerodynamic characteristics in insect flight, which is also required in advanced flapping micro aerial vehicles. The vortex-pairing and vortex-staying phenomena observed in this work provide an important clue to understanding the generation of aerodynamic force for rapid maneuverability.

Motion-Component Effects

Each motion component is extracted from the figure-eight motion, and the role of each motion component in aerodynamic-force generation is examined in the forward-flight condition. As mentioned previously, figure-eight motion is composed of translation, lagging, and rotation. Figures 13 and 14 show the history of lift and thrust coefficients. Figure 15 shows motions of the translational and lagging modes and the rotation-only modes.

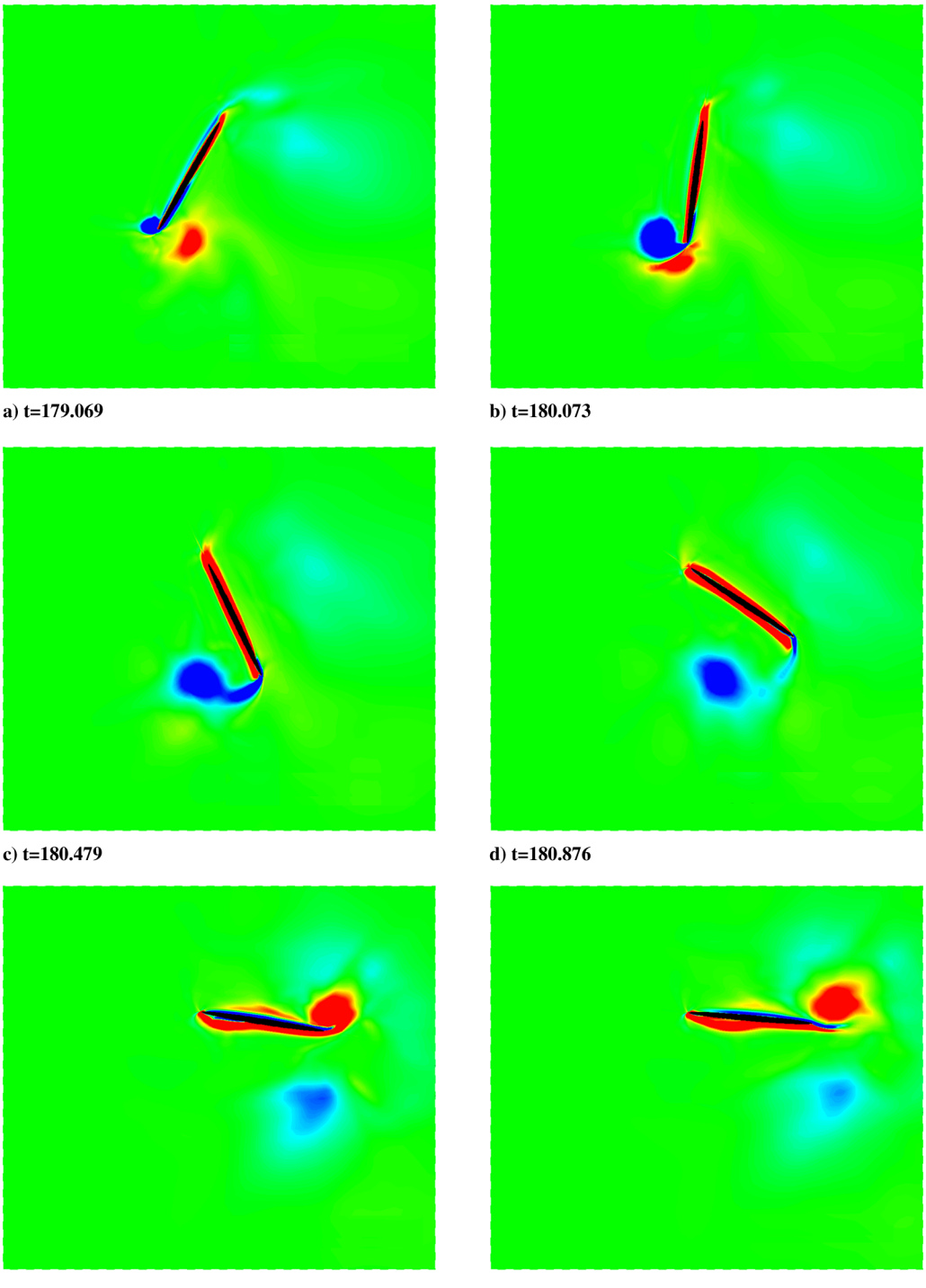

a) t=179.069 **b) t=180.073**

c) t=180.479 **d) t=180.876**

e) t=182.081 **f) t=182.683**

Fig. 16 Vorticity contours with rotational motion only.

During downstroke, the lift-generation pattern of translation/lagging is quite similar to that of translation/lagging/rotation, whereas remarkable differences exist during upstroke. In addition, rotation-only motion does not contribute much in lift generation (Fig. 13). This is consistent with the previous observation that an effective angle of attack for lift generation is exclusively dependent on translational and lagging velocity components. Compared with translation/lagging/rotation, the lift history of rotation-only motion is much less fluctuating and the overall lift pattern is quite different, except at the end of upstroke. However, thrust history (see Fig. 14) shows a noticeable resemblance: a large amount of thrust is generated abruptly at the end of upstroke, even with rotation only.

Figure 16 shows the flow features by rotational motion only. As the airfoil begins to rotate (Fig. 16a), a clockwise vortex sheds from the trailing edge (Figs. 16b and 16c). Because this vortex is created from the abrupt start of rotation, it may be called the *rotational starting vortex* (RSV), as described in hovering flight by Birch and Dickinson [25] The RSV very much resembles the staying vortex, as shown in Fig. 8. The RSV maintains a lower-pressure region at the lower surface of the airfoil and creates a substantial pressure difference across the airfoil surface, which provides thrust generation at the end of upstroke. In Fig. 16e, when rotation stops, a new counterclockwise vortex is created and the two vortices form a pairing, as in Fig. 9. Therefore, it is confirmed that the rotational component of figure-eight motion essentially provides the vortex-pairing and vortex-staying mechanisms for the abrupt thrust generation of figure-eight motion.

Rotational Circulation

From the previous analysis, it is seen that the rotational motion is the most important component of figure-eight motion to generate thrust. The relationship between rotation and aerodynamic-force generation can be clarified from the viewpoint of circulation. The history of angular velocity is compared with that of aerodynamic-force generation, because angular velocity is the physical quantity most closely related to wing rotation. In Fig. 17, behaviors of lift coefficient and angular velocity are not similar, except near the end region of upstroke. This is expected, because lift is mainly produced by a high effective angle of attack due to translational and lagging velocity components. However, as shown in Figs. 18 and 19, the angular velocity history is very similar to the thrust coefficient history. Recalling the results of Figs. 13, 14, and 16, this is not surprising at all.

As observed by Dickinson et al. [13], a rotating airfoil with some angular velocity provides a rotational circulation to the surrounding flowfield. For a thin airfoil such as an insect wing, the rotational circulation Γ_r can be defined as

$$\Gamma_r = \pi\omega c^2(0.75 - x_0) \tag{11}$$

In this work, counterclockwise direction is assumed to be positive. From Eq. (11), the rotational circulation depends on the wing chord and normalized position of the rotation center x_o. To find the physical role of the rotational circulation, additional numerical simulations are conducted for five cases (from $x_o = 0.1$ to 0.5).

Figures 20 and 21 show the change of lift and thrust patterns in terms of a rotation center x_o. The amplitude of lift and thrust is generally increasing as the rotation center moves to the leading edge or the magnitude of the rotational circulation increases, as in Eq. (11). As in Fig. 21, strong counterclockwise (positive) rotational circulation yields a positive thrust coefficient [from Eq. (11), the sign of the angular velocity and the rotational circulation is the same]. This characteristic is conspicuous at the end of upstroke. On the other hand, an opposite behavior is observed in the case of lift generation. In Fig. 20, the positive (or negative) rotational circulation induces the negative (or positive) lift generation, especially near the end of upstroke. Therefore, the counterclockwise rotational circulation promotes thrust generation but discourages lift generation. Figure 22 shows the relationship between the rotational circulation and mean thrust generation. The mean thrust coefficient is clearly proportional

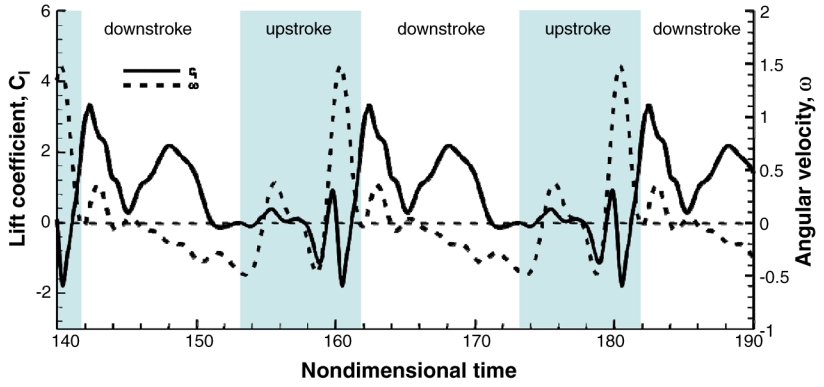

Fig. 17 Lift coefficient and angular velocity history (figure eight).

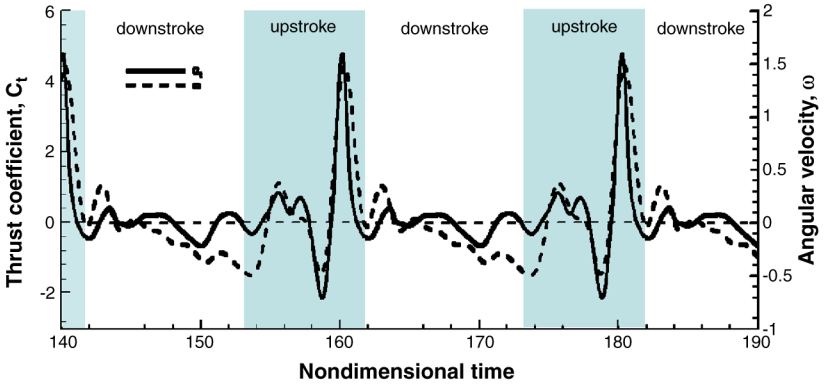

Fig. 18 Thrust coefficient and angular velocity history (figure eight).

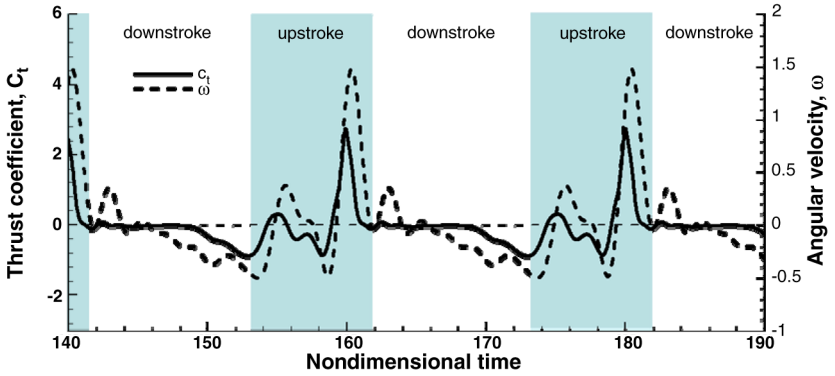

Fig. 19 Thrust coefficient and angular velocity history (rotation only).

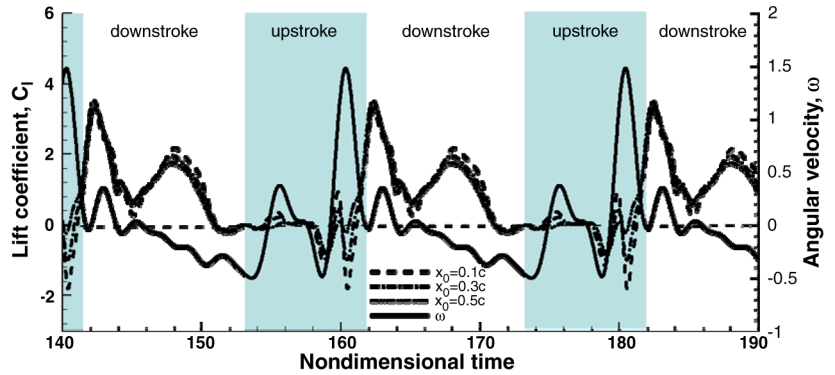

Fig. 20 Lift coefficient and angular velocity history (figure eight).

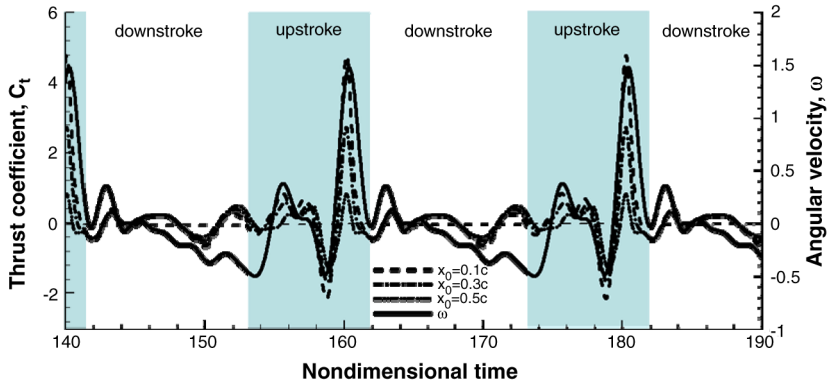

Fig. 21 Thrust coefficient and angular velocity history (figure eight).

to the rotational circulation. As the rotational center moves toward the airfoil center [0.75 from Eq. (11)], the rotational circulation with a given angular velocity is decreasing, and thus the mean thrust coefficient is also decreasing. Moreover, similar behavior is also observed in rotation-only motion in Fig. 23.

Based on the previous discussion and observation, Figs. 24 and 25 graphically summarize physical phenomena of the unsteady lift and thrust generation of figure-eight motion under the forward-flight condition. Basically, lift is produced by the clockwise circulation induced by the translational starting vortex that develops at the early stage of downstroke. As the TSV moves on the downstream side, the corresponding clockwise circulation develops at the airfoil. On the other hand, the airfoil rotation promotes the rotational circulation over the airfoil itself, and the opposite directional circulation is induced as a reaction. Thus, the clockwise RSV is generated from Figs. 8 and 16, which eventually takes part in the vortex staying and vortex pairing. It is also seen that the direction of the circulation for lift and thrust generation is opposite to each other. When the airfoil rotates rapidly at the end of upstroke, the lift and thrust pattern is

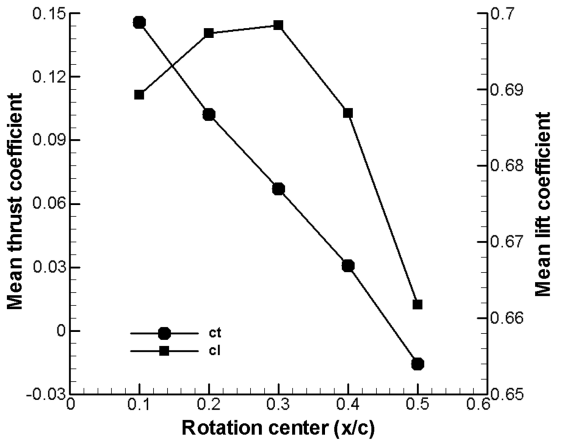

Fig. 22 Mean thrust and lift coefficient (figure eight).

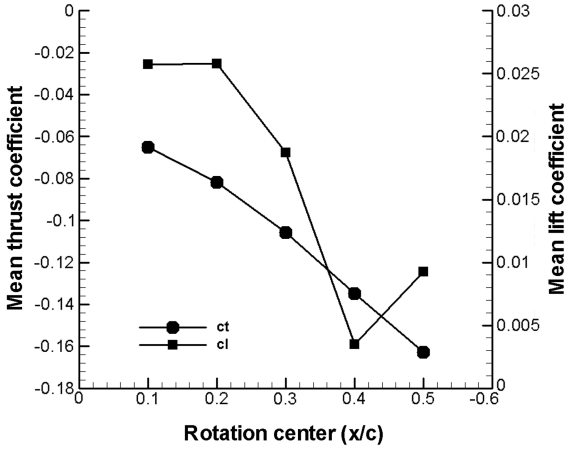

Fig. 23 Mean thrust and lift coefficient (rotation only).

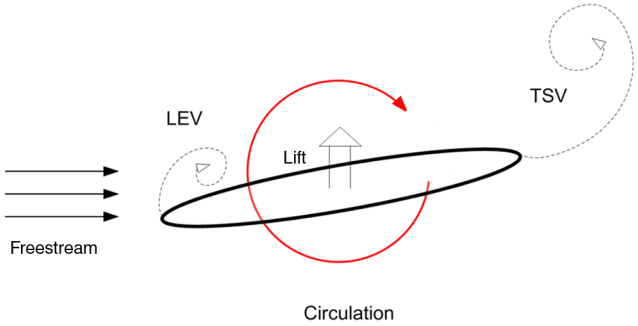

Fig. 24 Schematic summary of lift generation (clockwise circulation).

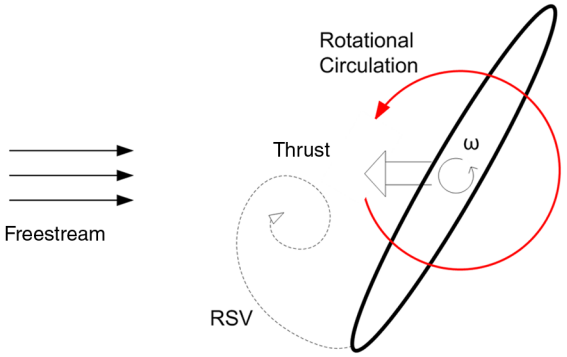

Fig. 25 Schematic summary of thrust generation (counterclockwise rotational circulation).

exactly the opposite (see Figs. 17 and 18), which can be easily explained using Figs. 24 and 25.

By beneficially exploiting the rotational circulation, the unsteady aerodynamic-force generation in figure-eight motion could be controlled. In addition, the newly uncovered flow physics may give an important clue to understanding the rapid maneuverability of insect flight and may be usefully applied in the design of flapping micro aerial vehicles.

Conclusions

Computations of unsteady viscous incompressible flows over a thin elliptical airfoil are carried out to investigate the unsteady aerodynamics of 2-D figure-eight motion under the forward-flight condition. Wing trajectory is extracted from data of the tethered-flight experiment by Nachtigall [16] of a blowfly under freestream.

Through extensive numerical results and detailed comparisons, it is observed that lift is mainly generated during downstroke by a high effective angle of attack due to translational/lagging motion. A strong translational starting vortex by a high effective angle of attack induces clockwise circulation around the airfoil, and it is responsible for most of lift generation. On the other hand, a large amount of thrust is generated abruptly at the end of upstroke. Computed flowfields show that vortex-pairing and vortex-staying mechanisms play a key role in the abrupt large thrust generation. When the airfoil rapidly rotates at the end of upstroke, a RSV develops from the airfoil shear layer as a reaction to rotational circulation around the airfoil and it joins in vortex staying and vortex pairing. Through analyses on the effect of motion component, rotation turns out to be the most important component in thrust generation. Rotational circulation (counterclockwise circulation) due to airfoil rotation promotes thrust generation but prevents lift generation.

Together with hovering, rapid maneuvering is one of the most distinguishable flight capabilities of insect flight. The vortex-pairing and vortex-staying phenomena observed in figure-eight motion provide an important clue to understanding the rapid maneuvering of insect flight, and they could be usefully applied to the design of flapping micro aerial vehicles.

Acknowledgments

This work was supported by the Brain Korea 21 Project and by grant R01-2005-000-10059-0 from the Basic Research Program of the Korea Science and Engineering Foundation. The authors also gratefully acknowledge the financial support of the Agency for Defense Development and by the Flight Vehicle Research Center (FVRC), Seoul National University.

References

[1] Koochesfahani, M. M., "Vortical Patterns in the Wake of an Oscillating Airfoil," *AIAA Journal*, Vol. 27, No. 9, Sept. 1989, pp. 1200–1205.

[2] Anderson, J. M., Streitlien, K., Barrett, D. S., and Triantafyllou, M. S., "Oscillating Foils of High Propulsive Efficiency," *Journal of Fluid Mechanics*, Vol. 360, No. 1, 1998, pp. 41–72. doi:10.1017/S0022112097008392

[3] Isogai, K., Shinmoto, Y., and Watanabe, Y., "Effect of Dynamic Stall on Propulsive Efficiency and Thrust of Flapping Foil," *AIAA Journal*, Vol. 37, No. 10, Oct. 1999, pp. 1145–1151.

[4] Tuncer, I. H., and Platzer, M. F., "Computational Study of Flapping Airfoil Aerodynamics," *Journal of Aircraft*, Vol. 37, No. 3, May 2000, pp. 514–520.

[5] Mustafa, K., and Tuncer, I. H., "Nonsinusoidal Path Optimization of a Flapping Airfoil," *AIAA Journal*, Vol. 45, No. 8, Aug. 2007, pp. 2075–2082. doi:10.2514/1.29478

[6] Lee, J. S., Kim C., and Kim, K. H., "A Design of Flapping-Airfoil for Optimal Aerodynamic Performance in Low Reynolds Number Flows," *AIAA Journal*, Vol. 44, No. 9, 2006, pp. 1960–1972. doi:10.2514/1.15981

[7] Platzer, M. F., and Jones, K. D., "Flapping Wing Aerodynamics—Progress and Challenges," AIAA Paper 2006-500, 2006.

[8] Rozhdestvensky, K. V., and Ryzhov, V. A., "Aerohydrodynamics of Flapping-Wing Propulsors," *Progress in Aerospace Sciences*, Vol. 39, No. 8, 2003, pp. 585–633. doi:10.1016/S0376-0421(03)00077-0

[9] Ennos, R., "Unconventional Aerodynamics," *Nature*, Vol. 344, Apr. 1990, p. 491. doi:10.1038/344491a0

[10] Ellington, C. P., van den Berg, C., Willmott, A. P., and Tomas, A. L. R., "Leading-Edge Vortex in Insect Flight," *Nature*, Vol. 384, Dec. 1996, pp. 626–630. doi:10.1038/384626a0

[11] Ward-Smith, A. J., *Biophysical Aerodynamics and the Natural Environment*, Wiley, New York, 1984.

[12] Sun, M., and Yu, X., "Aerodynamic Force Generation in Hovering Flight in a Tiny Insect," *AIAA Journal*, Vol. 44, No. 7, 2006, pp. 1532–1540. doi:10.2514/1.17356

[13] Dickinson, M. H., Lehmann, F., and Sane, S. P., "Wing Rotation and the Aerodynamic Basis of Insect Flight," *Science*, Vol. 284, No. 5422, 1999, pp. 1954–1960. doi:10.1126/science.284.5422.1954

[14] Lehmann, F., "The Mechanisms of Lift Enhancement In the Insect

Flight," *Die Naturwissenssenschaften*, Vol. 91, No. 3, 2004, pp. 101–122.
doi:10.1007/s00114-004-0502-3

[15] Sane, S. P., "The Aerodynamics of Insect Flight," *Journal of Experimental Biology*, Vol. 206, No. 23, 2003, pp. 4191–4207.
doi:10.1242/jeb.00663

[16] Nachtigall, W., *Insects in Flight*, McGraw–Hill, New York, 1974.

[17] Wang, Z. J., "Dissecting Insect Flight," *Annual Review of Fluid Mechanics*, Vol. 37, 2005, pp. 183–210.
doi:10.1146/annurev.fluid.36.050802.121940

[18] Sun, M., and Lan, S. L., "A Computation Study of the Aerodynamic Forces and Power Requirements of Dragonfly (Aeshna Juncea) Hovering," *Journal of Experimental Biology*, Vol. 207, No. 11, 2004, pp. 1887–1901.
doi:10.1242/jeb.00969

[19] Rosers, S. E., and Kwak, D., "An Upwind Differecing Scheme for the Time-Accurate Incompressible Navier-Stokes Equations," *AIAA Journal*, Vol. 28, No. 2, 1990, pp. 253–262.

[20] Kim, C. S., Kim, C., and Rho, O. H., "Parallel Computations of High-Lift Airfoil Flows Using Two-Equation Turbulence Models," *AIAA Journal*, Vol. 38, No. 8, 2000, pp. 1360–1368.

[21] Brodsky, A. K., *The Evolution of Insect Flight*, Oxford Univ. Press., Oxford, 1994.

[22] Lee, J. S., "Numerical Study on Flapping-Airfoil Design and Unsteady Mechanism of Two-Dimensional Insect Wing," Ph.D. Thesis, Seoul National Univ., Seoul, Republic of Korea, 2006.

[23] Wilkins, P., and Knowles, K., "Investigation of Aerodynamics Relevant to Flapping-Wing Micro Air Vehicles," AIAA Paper 2007-4338, 2007.

[24] Lugt, H. J., *Vortex Flow in Nature and Technology*, Wiley, New York, 1983.

[25] Birch, J. M., and Dickinson, M. H., "The Influence of Wing-Wake Interaction on the Production of Aerodynamic Force in Flapping Flight," *Journal of Experimental Biology*, Vol. 206, No. 13, 2003, pp. 2257–2272.
doi:10.1242/jeb.00381

A. Plotkin
Associate Editor